ACS APPLIED NANO MATERIALS

www.acsanm.org Article

Atomically Dispersed Pt on TiO_2 Nanosheets for Catalytic Gaseous Acetaldehyde Abatement

Asad Mahmood,* Xiao Wang, Xiaofeng Xie, and Jing Sun*

Cite This: *ACS Appl. Nano Mater.* 2021, 4, 3799−3810 Read Online

ACCESS | Metrics & More | Article Recommendations | Supporting Information

ABSTRACT: Increasing volatile organic compounds (VOCs) in the atmosphere have triggered intensive research on photocatalytic oxidation technology to safely photodegrade these volatile organic pollutants. Downsizing metal catalysts up to an atomic level on oxide supports can provide more active sites on the surface for different reactions, i.e., CO oxidation, CO_2 reduction, removal of organic pollutants as well as decrease the use of precious metals. Here, we designed atomically dispersed metal catalysts (ADMCs), i.e., Pt on TiO_2 nanosheets, which produced a robust and stable photocatalytic degradation of the gas-phase acetaldehyde. The loading of Pt was carried out using different deposition times, such as 2, 4, and 6 h, designated as Pt/T *x*h at 70 °C. This was followed by vacuum drying (60 °C) and subsequent calcination at 125 °C in an inert atmosphere. The high-angle annular dark-field scanning transmission electron microscopy (HAADF-STEM) analysis confirmed the presence of atomically dispersed Pt on TiO_2 nanosheets. The sample Pt/T 4h displayed a high photodegradation efficiency (100%) than pure TiO_2 (38%) for 500 ppm of acetaldehyde with a flow rate of 10 sccm. Also, 700 ppm of CO_2 was produced by Pt/T 4h in contrast to 340 ppm by pure TiO_2. The experimental data for the sample Pt/T 4h was further characterized using Langmuir−Hinshelwood kinetic models to determine the reaction rates, adsorption equilibrium constants, and water adsorption constant. This study provides a unique opportunity to develop metal-decorated TiO_2-based photocatalysts for the robust and efficient removal and mineralization of acetaldehyde from the indoor atmosphere.

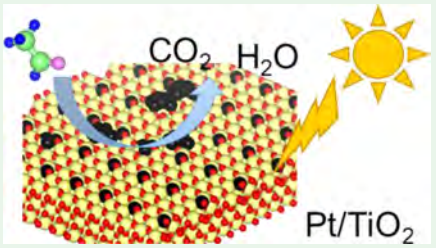

KEYWORDS: *photocatalysis, Pt-decorated TiO_2, acetaldehyde, HAADF-STEM, VOCs*

INTRODUCTION

Air pollution is a major cause of premature deaths and diseases (e.g., cardiac and respiratory) around the globe and is the single largest environmental health risk in many countries. In a recent report (EEA report no 10/2019), the European Environmental Agency attributed 400 000 premature deaths/year in EEA-39.[1] The main source of air pollution is the low boiling point (∼50 to 250 °C) volatile organic compounds (VOCs). VOCs are also accountable for the increasing ozone content in the troposphere and the formation of fine particulates via reactions with nitrogen oxides (NOx) and carbon monoxide (CO).[2,3] The concentration of VOCs in an indoor air environment is much higher (5−100 times) than that in the outdoors, which poses serious health risks. Several technologies including nonthermal plasma,[4] adsorption,[5] and photocatalytic oxidation (PCO)[6−8] have been developed to address this issue. Photocatalytic oxidation (PCO) is a promising technology to eliminate indoor air pollutants including VOCs.[9−12] Despite investigations on various oxide-based semiconductors, TiO_2 is still the focus of interest due to its abundance, nontoxicity, and oxidizing properties.[13−16] Recent progress on metal-oxide growth strategies suggests that the growth of metal catalysts on oxide supports might result in an interface, where the metal-to-metal bonds are of similar strength as the metal-to-oxide bonds.[17−21] Thus, a strong metal−support interaction is established when the metal nanoparticles are partially covered by the oxide support on reduction.[22] Reducible oxide-based semiconductors, e.g., TiO_2, Cu_2O, FeO_x, and CeO_2 are suitable supports for developing atomically dispersed metal catalysts (ADMCs) by incorporating precious metals i.e., Pt, Pd, and Au. This technique generates more reactive sites and ensures the cost-effective use of precious metals. The superior photocatalytic performance of ADMCs can be attributed to many factors, including the production of high-energy electrons in metals under light illumination, which activate molecules on the surface. Additionally, the light absorption capability of metal nanoparticles is greater than oxide-based semiconductors. Accordingly, Pt-modified TiO_2 has been widely studied for the photodegradation of VOCs; however, ADMCs are ignored for the gas−solid photocatalysis.[23,24]

In this article, we studied atomically dispersed Pt cocatalyst on TiO_2 nanosheets, predominantly grown along the <001>

Received: January 24, 2021
Accepted: March 30, 2021
Published: April 7, 2021

https://doi.org/10.1021/acsanm.1c00208
ACS Appl. Nano Mater. 2021, 4, 3799−3810

Scheme 1. Synthesis of Pure and Atomically Dispersed Pt on TiO_2 Nanosheets

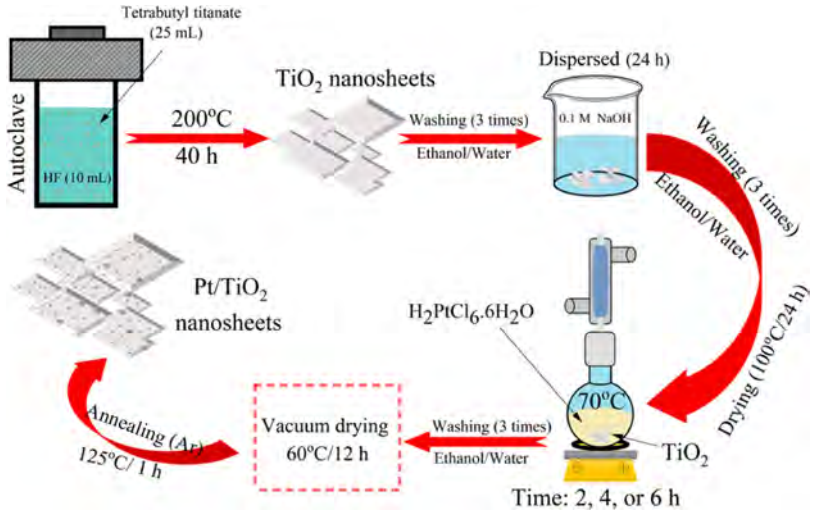

direction. TiO_2 nanosheets with an exposed (001) surface are preferred due to their high surface energy (0.90 Jm^{-12}), the under-coordination of surface Ti_{5c} (5-fold Ti atoms) and O_{2c} (2-fold oxygen atoms), and their superior photocatalytic activity.[25,26] For example, Yu et al.[27] studied the effect of TiO_2{001} and {101} facets on the photoreduction of CO_2. Detailed density functional theory (DFT) calculations showed that the Fermi level of {001} facets enters their valence band (VB). On the contrary, the Fermi level of {101} facets is located at the top of the VB. The contact between the {001} and {101} facets will form a surface heterojunction, which is anticipated to improve the hole−electron separation. The ratio of {001} and {101} facets was controlled using different hydrofluoric acid (HF) contents (HF: 0 (11% {001} facets) to 9 mL (83%; {001} facets)) under hydrothermal reaction conditions. The photocatalytic activity of the as-prepared TiO_2 nanoparticles was studied during CO_2 photoreduction. The results showed that TiO_2 nanoparticles with a low {001} percentage (11%; no HF) exhibited a poor CH_4 production rate (0.15 μmol h^{-1} g^{-1}). When the HF content was increased from 3 (49%; {001} facets) to 4.5 mL (58%; {001} facets), a significant increase in the CH_4 production rate was observed, exhibiting 0.75 μmol h^{-1} g^{-1} and 1.35 μmol h^{-1} g^{-1}, respectively. Further increase in the TiO_2{001} facet % decreased the CH_4 production from 0.82 μmol h^{-1} g^{-1} (HF = 6mL) to 0.55 μmol h^{-1} g^{-1} (HF = 9 mL). This study suggested that initially the hole−electron separation was improved due to an optimum ratio of {001} and {101} facets, e.g., HF = 4.5 mL ({001} = 58%). As the percentage of {001} facets increased, the photocatalytic activity was observed to decrease due to the electron overflow effect from {001} facets to {101} facets. Due to the large percentage of {001} facets, the transfer of electrons was impeded from {001} to {101} facets and thus, recombination of these electrons within the {001} facets occurred simultaneously. The TiO_2 nanosheets were synthesized under strong acidic hydrothermal conditions. Photocatalytic oxidation and mineralization efficiency of gas-phase acetaldehyde was carried out under UV−visible light illumination using an automatic flow reactor coupled with gas chromatography (GC) to monitor the degradation process. Acetaldehyde is a major indoor air pollutant that is introduced into the atmosphere from various sources, for example, building materials, synthetic materials, and domestic chemistry.[28] It is a well-known human carcinogen, which has been regulated on a priority basis in EU, China, and the USA.[29] Pt-modified TiO_2 nanosheets efficiently photodegraded acetaldehyde at room temperature, whereas pure TiO_2 showed poor performance. The efficient photodegradation is attributed to the good light-harvesting capability and improved charge separation process in Pt-modified TiO_2 nanosheets. Moreover, the presence of Pt facilitated the mineralization efficiency of acetaldehyde to a great extent. The gas−solid reaction mechanism was further rationalized using several Langmuir−Hinshelwood kinetic equations to determine the reaction rate, adsorption equilibrium constant, and water adsorption constant.

EXPERIMENTAL SECTION

Synthesis of TiO_2 Nanosheets. TiO_2 nanosheets were grown along the (001) plane through a modified hydrothermal method.[6] In the first step, tetrabutyl titanate (25 mL, Sigma-Aldrich, 97%) and HF (10 mL, Sigma-Aldrich, 40% aqueous solution) were mixed in a dry Teflon-lined autoclave reactor and treated at 200 °C for 40 h. The as-prepared precipitates were thoroughly washed with deionized water and absolute ethanol. The product was dispersed in 0.1 M NaOH (Sigma-Aldrich, ≥97%) solution for 24 h and subsequently washed with deionized water and dried at 100 °C in an electric furnace. Finally, the powders were washed three times with deionized water and absolute ethanol before being dried (100 °C) in an electric furnace for 24 h.

Synthesis of Pt-Decorated TiO_2 Nanosheets. Deposition of Pt was carried out in a round bottom flask (250 mL) using a thermal deposition method.[19] Initially, 0.5 g of TiO_2 nanosheets was dispersed in deionized water (100 mL) and sonicated for 2 h. The container was transferred to an oil bath and maintained at 70 °C. A predetermined amount of $H_2PtCl_6{\cdot}6H_2O$ was dissolved in 2 mL of deionized water, which was added to the TiO_2 dispersion container and magnetically stirred on a hot plate (70 °C) for different times, e.g., 2, 4, and 6 h. As a control, pure TiO_2 was processed under similar conditions without adding the Pt source. The as-prepared slurry was centrifuged at 1000 rpm for 10 min and washed three times with deionized water. The samples were dried in a vacuum furnace at 60 °C overnight. Finally, the powders were calcined in a tube furnace at 125 °C for 1 h under an argon atmosphere. Hence, TiO_2 nanosheets decorated with 0.053, 0.097, and 0.231 wt % Pt were achieved. These parameters were determined by inductively coupled plasma-atomic emission spectroscopy. The samples decorated with Pt at different time intervals are designated as the following: Pt/T *x*h, where Pt demonstrates the Pt-decorated sample, T is TiO_2, and *x*h shows the number of hours. For

https://doi.org/10.1021/acsanm.1c00208
ACS Appl. Nano Mater. 2021, 4, 3799−3810

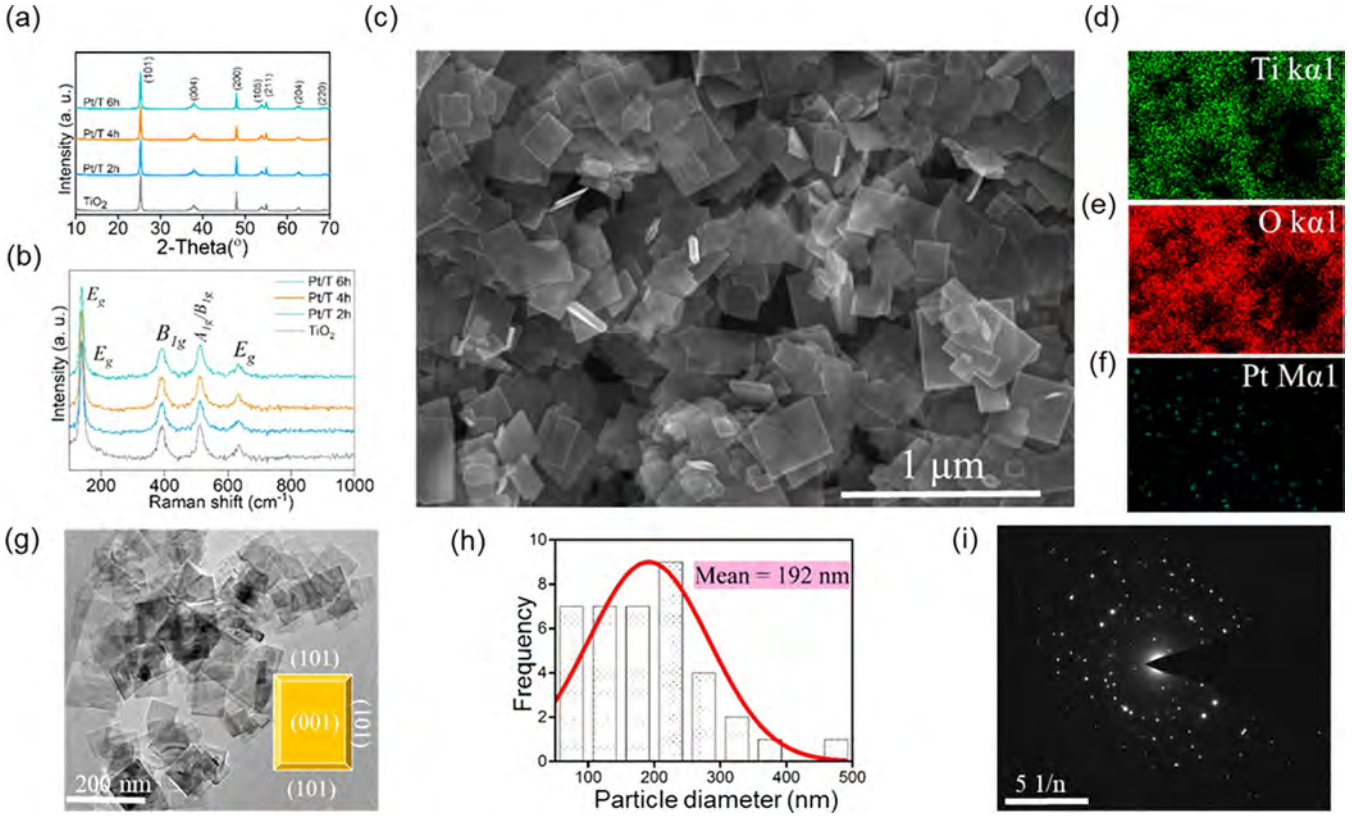

Figure 1. Phase and microstructure analysis of pure and Pt-modified TiO_2 nanosheets. XRD (a) and Raman spectroscopy (b). FESEM (c) and the corresponding EDS mapping of Pt/T 4h showing the dispersion of Ti (green), O (red), and Pt (cyan), (d, e, f). TEM analysis and mean particle diameter of Pt/T 4h, TEM image (g), particle size distribution (h), and SAED (i).

instance, Pt/T 2h indicates the deposition process of Pt on TiO_2 carried out for 2 h. The overall synthesis process can be viewed in Scheme 1. Pt nanoparticles were prepared by the wet impregnation technique. TiO_2 nanoparticles were mixed with H_2PtCl_6 (same amount as for Pt) under constant stirring at room temperature for 6 h. The as-prepared slurry was dried at 100 °C in an oven. The sample was calcined at 400 °C (step size 5 °C min^{-1}), which was further treated at 250 °C for 1 h in a tube furnace (H_2 flow). Lastly, H_2 gas was replaced with N_2 gas for an additional hour to remove adsorbed H_2.

Spectral Characterization. The X-ray diffraction (XRD) study was performed using an Ultima IV 2036E102 (Rigaku Corporation, Japan) X-ray diffractometer with a Cu Kα1 source (λ = 0.15406 nm). The Raman study was carried out using a DXR Raman microscope (Thermo Fisher Scientific) utilizing a laser with an excitation wavelength of 532 nm at 7 mW laser power. The surface morphology was investigated using a field-emission scanning electron microscope (FESEM; JEOL JSM-6700F). The microstructure analysis was carried out using a high-resolution transmission electron microscope (TEM JEOL 2100) operating at 200 kV coupled with a LaB6 source. Gatan Orius charge-coupled devices were used to collect the high-resolution TEM (HRTEM) images. The high-angle annular dark-field (HAADF) images were acquired with a probe-corrected scanning transmission electron microscope HF5000 (Hitachi High-Tech, Japan) working at 200 kV. The optical absorption study was performed using a UV/vis/NIR spectrophotometer (Perkin Elmer Lambda 950). The photoluminescence (PL) study was performed using a Perkin Elmer luminescence spectrometer C 55 at an excitation wavelength of 320 nm. The Brunauer–Emmett–Teller specific surface area (BET_{SSA}) of the samples was analyzed using a nitrogen desorption isotherm apparatus (Micrometrics ASAP 3000). Prior to experiments, the samples were degassed at 120 °C for 24 h. The X-ray photoelectron spectroscopy (XPS) analysis was performed using a Thermo K-Alpha spectrometer (Thermo scientific ESCALAB 250Xi) with monochromatic Al K-Alpha radiation, which is a dual-beam charge compensation system with a constant pass energy of 50 eV. Survey scans were collected in the range of 0–1200 eV. The XPS peaks were further fitted to identify the nature of elements present in the samples. Ultraviolet photoelectron spectroscopy (UPS) was carried out to determine the surface work function using a Thermo ESCALAB250 XI (He^I = 21.2 eV; passing energy = 5.0 eV). A model JES-FA200 spectrometer was used to conduct the electron spin resonance (ESR) experiment to trace the production of oxide radicals. In the ESR study, 5,5-dimethyl-1-pyrroline *N*-oxide (DMPO; DOJINDO Lab; >99%) was used as a radical trapping agent. The scavenger experiment was conducted using radical scavengers, which include *p*-benzoquinone (PBQ) and (2,2,6,6-tetramethyl-1-piperidinyloxy (TEMPO) for $^{\bullet}O_2^-$ and $^{\bullet}OH$ radicals, respectively. The electron paramagnetic resonance (EPR) study was carried out at room temperature operated at an X-band frequency (9.069 GHz) and 100 kHz field modulation. The photocurrent study was performed using a CHI660D electrochemical workstation in a conventional three electrode cell configuration that includes Ag/AgCl as the reference electrode, Pt as the counter electrode, and samples coated on FTO as the working electrode.

Dynamic Adsorption–Desorption and Photodegradation Test. To test the photocatalytic activity of the pure and Pt-modified TiO_2 samples for the gas-phase photodegradation of acetaldehyde, the dynamic adsorption–desorption and photodegradation experiments were performed in an automated gas circulation reaction chamber coupled with gas chromatography. Initially, the photocatalyst sample (0.1 g) was mixed-milled in 10 mL of absolute ethanol using a mortar and pestle for 10 min. The as-prepared slurry was drop-cast on a glass substrate (16 × 13 cm) and subsequently dried in air. The samples were further dried (60 °C) using a vacuum oven for 1 h. The as-prepared samples were transferred to a reaction chamber, which was tightly sealed. Acetaldehyde (1000 ppm) and compressed air (1000 ppm) were allowed to flow through the sample-holding reaction

https://doi.org/10.1021/acsanm.1c00208
ACS Appl. Nano Mater. 2021, 4, 3799–3810

chamber and the process was monitored through GC. After achieving the adsorption−desorption equilibrium in the dark, the samples were irradiated using a 400W xenon lamp with an illumination density of 80 mW/cm^2 measured with a THORLABS GmbH (PM100D; S314C detector) as the radiation source. Fresh samples were used for every experiment excluding the cyclic test. The reaction was also performed without using any photocatalysts (blank chamber).

Computational Details. The periodic density functional theory study was performed using the Vienna ab-initio simulation package (VASP).[30−32] The crystal lattice of three-dimensional TiO_2 was fully relaxed using a 2 × 2 × 1 supercell. Structure optimization and property calculations were carried out using generalized gradient approximation (GGA) as an exchange-correlation function given by Perdew−Burke−Erzhenhof (PBE).[33] The noncovalent interactions were accounted for using the van der Waals (vdW) correction method (DFT−D3 framework) implemented by Grimme, which utilizes a simple pairwise force field to describe the vdW forces.[34] The fully relaxed TiO_2 was cleaved along two directions (101) and (001) to mimic the desired TiO_2 surfaces. A vacuum of 20Å was used for the slab models. Constraints were applied to the bottom three layers of the slabs to mimic the bulk and surface character during the computations. Different positions of the Pt atoms were tested to comprehend the interaction of Pt atoms on the surface, bond distance, and stability. In all of the computations, a cutoff energy of 520 eV was used. The Brillouin zone was sampled with the Monkhorst−Pack mesh 5 × 5 × 1 grid in the reciprocal space. The partial density of states (PDOS) was calculated to study the electronic structure of pure and Pt-modified TiO_2 surfaces.

RESULTS AND DISCUSSION

Phase and Microstructure Analysis. TiO_2 nanosheets with an exposed (001) surface were synthesized using a hydrothermal method. The loading of Pt was carried out using different deposition times, e.g., 2, 4, and 6 h designated as Pt/T *x*h at 70 °C using a round bottom flask containing TiO_2 nanosheets and $H_2PtCl_6{\cdot}6H_2O$. This was followed by vacuum drying (60 °C) and subsequent calcination at 125 °C in an Ar atmosphere. X-ray diffraction (XRD) and Raman spectroscopy confirm the anatase phase with no considerable difference in lattice parameters by Pt decoration (Figure 1a,b and Table S1).[35,36] The FESEM micrograph shows a sheet-like morphology (nanosheets), which is similar to the TiO_2 nanoparticles predominantly grown along the <001> direction (Figure 1c). The percentage of the (001) surface is calculated to be ∼84% (Figure S1).[37] The energy-dispersive X-ray spectroscopy (EDS) analysis confirmed Ti, O, and Pt as the main elements (Figure 1d−f). The TEM results additionally validate the morphology in more depth (Figure 1g), with a mean particle size of ∼192 nm (Figure 1h). The top surface of TiO_2 nanosheets is regarded as the (001) surface while the sides of the particles are the (101) surface (inset sheet model). The selected area electron diffraction (SAED) pattern shows evidence of the well-crystalline nature of the particles (Figure 1i).

The TEM image reveals small Pt nanoparticles (Figure 2a,b). The particles are dominantly aggregated on the edges of the nanosheets while the top surface incorporated a small quantity. This behavior could possibly be due to the exclusive behavior of TiO_2 surfaces, which dominantly include (101) and (001) in this case. As a result of the difference in the atomic arrangement and surface energy of the TiO_2(101) and (001) surfaces, the aggregation of Pt atoms on these facets is unique. The surface energy of TiO_2(001) is 0.9 Jm^{-12}, which is higher than TiO_2(101) (0.44 Jm^{-12}). This could be due to the strong metal−support interaction (Pt−O in this case), which

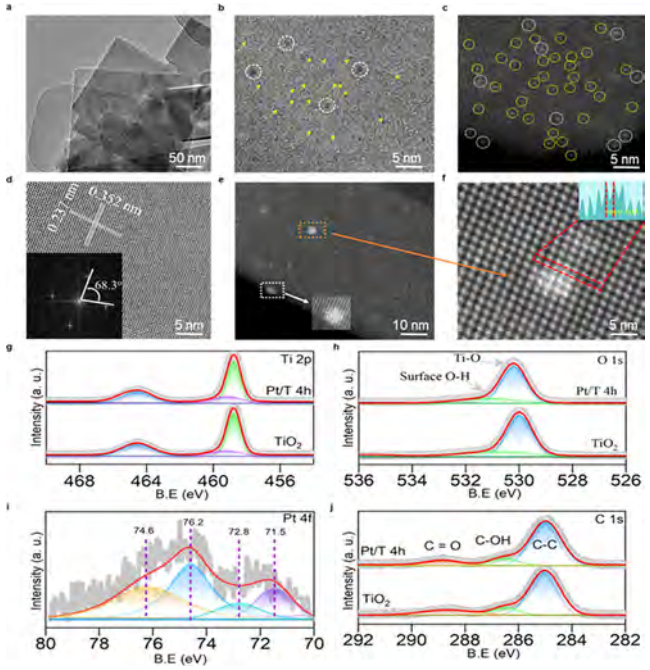

Figure 2. HRTEM, HAADF-STEM images, and XPS analysis of Pt/T 4h. HRTEM image of the particle morphology at high resolution (a). HRTEM of Pt distribution on the TiO_2 surface (b), white circles indicate large clusters while yellow arrows show small clusters or monodispersed atoms. HAADF-STEM images; isolated Pt atoms are encircled yellow while small clusters are highlighted in white circles (c), and surface features and the FFT image (d), surface micrograph of Pt agglomerates and single atoms (e), and isolated Pt agglomerated on the TiO_2(001) surface (f). XPS analysis; Ti 2p spectra (g), O 1s spectra (h), Pt 4f spectra (i), and C 1s spectra (j).

renders stability and immobility to the Pt atoms on the TiO_2 surface, thus inhibiting the agglomeration of Pt atoms for the most part. To test this hypothesis, we carried out periodic DFT calculations of Pt adsorption on TiO_2(101) and (001) surfaces. These results confirm that there are strong interactions between the TiO_2(001) surface and Pt than Pt on the TiO_2(101) surface. These findings are further discussed in the Photocatalytic Degradation and Mineralization of Acetaldehyde section, which suggests that atomically dispersed Pt can be formed at this relative annealing temperature (125 °C). The Pt on the surface shows a narrow size distribution (average value = 0.35 nm: Figure S2). The high-angle annular dark-field scanning transmission electron microscopy (HAADF-STEM) results demonstrate high-resolution structural dynamics of the Pt growth on TiO_2 nanoparticles (Figure 2c−f). Monodispersed Pt atoms can be clearly traced even though both the pure and Pt-modified TiO_2 samples were treated at 125 °C for 1 h (Figure 2c). To confirm the role of F ions in the surface morphology of the Pt atoms, we prepared a fresh sample and completely removed the surface F ions. The Pt was decorated for 4 h under similar conditions given in the Experimental section. The HAADF-STEM analysis displayed a similar behavior for the Pt atoms (Figure S3), as anticipated in the sample Pt/T 4h (Figure 2c,e). Thus, it can be inferred that the surface fluorides did not play a significant role in the surface distribution of Pt. This could be associated with the fact that most of the surface F ions were deliberately removed by quenching TiO_2 nanosheets in 0.1 M NaOH before Pt deposition.

https://doi.org/10.1021/acsanm.1c00208
ACS Appl. Nano Mater. 2021, 4, 3799−3810

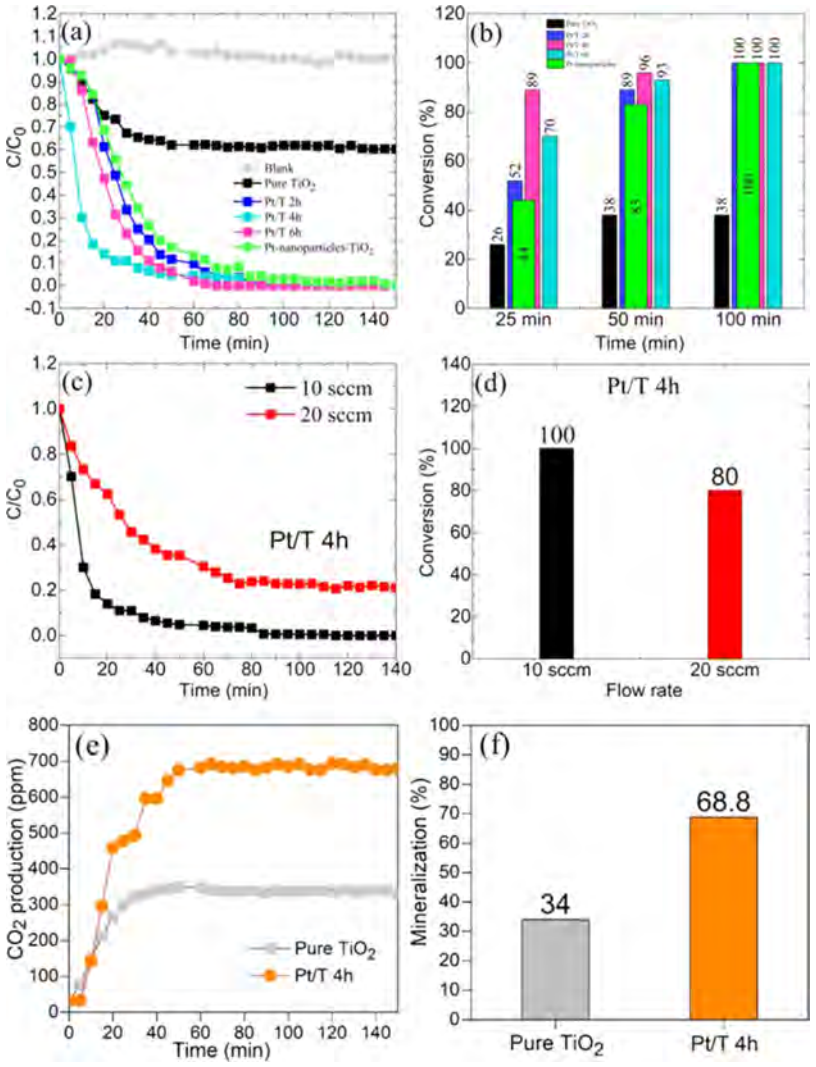

Figure 3. Photodegradation of gas-phase acetaldehyde on pure and Pt-modified TiO_2 nanosheets (a) and comparative conversion efficiencies after different time intervals (b). Conversion efficiencies at different flow rates (c, d). Mineralization curves (e) and efficiencies (f) of pure TiO_2 and Pt/T 4h in the course of gas-phase acetaldehyde photodegradation.

Also, small clusters of Pt coexist in this sample with a varying number of atoms. Figure 2d shows the HAADF-STEM image of the sample Pt/T 4h of a different location. The measured lattice fringes 0.237 and 0.352 nm correspond to the TiO_2(001) and (101) surfaces, respectively. The inset of the FFT image demonstrates the characteristic surface angle (68.3°) of the anatase TiO_2(001) surface. Two structural dynamics are visible for these small clusters (Figure 2e,f). The clusters, which are present at the top surface (i.e., TiO_2(001)) display a relatively loosely bound conglomeration of atoms (Figure 2f) with an interatomic distance of 0.331 nm. This distance is larger than the Pt−Pt distance in PtO (0.31 nm) and in metallic Pt (0.276 nm).[38] In contrast, the Pt atoms present on the TiO_2(101) surface depict well-defined nanoclusters containing several atoms (Figure 2e inset). These outcomes further verified the HRTEM results that the nature of the TiO_2 surface plays a significant role in stabilizing the Pt atoms. Despite the formation of these small clusters, the surface predominantly shows the existence of monodispersed Pt atoms. The survey XPS spectra show Ti 2s, Ti 2p, Ti 3s, Ti 3p, O 1s, and C 1s peaks (Figure S4) while the convoluted peaks of Ti 2p, O 1s, Pt 4f, and C 1s are given in Figure 2. In Ti 2p, the two peaks are resolved at binding energy (BE) values of 467.77 and 466.55 eV for pure TiO_2 (Figure 2g).[39] The Ti^{4+} $2p_{3/2}$ peak in pure TiO_2 appears at a BE of 464.55 eV, which shifts to a high BE value (464.77 eV) for the Pt/T 4h sample. The shift to a higher BE value verifies an interaction between Pt and TiO_2. Similar results have been observed by Wei et al.[40] Their study on Au and Pt-modified TiO_2 demonstrate obvious changes in the BE of Ti 2p peaks toward low BE compared to pure TiO_2. The shift toward low BE was associated with the reduction of Ti^{4+} into Ti^{3+}. Although we did not observe such a significant shift, still a small variation in BE can be associated with the decoration of Pt on TiO_2. For example, Wan et al.[41] have reported no obvious changes in the Ti 2p peaks by Au deposition. To further study the nature of surface defects, we carry out the EPR study of pure and Pt/T 4h samples (Figure S5). The presence of oxygen vacancies can be seen in both samples. Both samples did not show a significant difference. Two distinguished resonance peaks can be observed at g = 2.006 and 1.999, which are associated with the oxygen vacancy and Ti^{3+}, respectively.[42−44] The O 1s peak for pure TiO_2 (529.98 eV) shifts to 530.21 eV in the case of Pt/T 4h, which is attributed to the lattice oxygen (Ti−O)

https://doi.org/10.1021/acsanm.1c00208
ACS Appl. Nano Mater. 2021, 4, 3799−3810

Table 1. Kinetic Parameters Determined through Langmuir−Hinshelwood Kinetic Models for the Pt/T 4h Sample

	L−H kinetic models						
	model 1	model 2	model 3	model 4	model 5	model 6	model 7
	Parameters						
k (ppmv min^{-1})	0.069	0.015	0.0673	0.0672	0.1586		0.2329
K_A (ppmv^{-1})	0.5701	0.7547	2.1527	6.7295	0.7243		0.4196
K_W (ppmv^{-1})		0.00044	0.000185	0.000011	0.000074		0.00024
RSS	0.000213	0.000161	0.000161	0.000161	0.000148		0.000346
R^2	0.89	0.92	0.92	0.92	0.93		0.85

(Figure 2h).[45] Despite the large number of scanning cycles (16), the Pt 4f produced a noisy spectrum that can be ascribed to the low weight percent (Figure 2i). The Pt peak fitting confirmed two Pt species (i.e., Pt^{2+} and Pt^{o+}). The peaks at BE values of 76.2 and 72.8 eV are associated with the Pt^{2+} while the peak at 74.6 and 71.5 eV correspond to the Pt°. The C 1s spectrum displays three peaks at BE values, i.e., 285.01, 286.49, and 288.65 eV, which are assigned to C−C, C−OH, and C═O bonds, respectively (Figure 2j).[46,47] The XPS results confirmed the presence and strong interaction of Pt on the TiO_2 surface.

Photocatalytic Degradation and Mineralization of Acetaldehyde. The photocatalytic activities of pure and Pt-modified TiO_2 nanosheets were studied in an automated reaction chamber coupled with a GC (Figure S6; schematic view). The empty chamber does not exhibit any apparent photodegradation of acetaldehyde (Figure 3a). In the presence of TiO_2, substantial photocatalytic activity is observed. TiO_2 displays high photodegradation activity in the beginning, which becomes progressively lower. When Pt-modified TiO_2 samples were used as the photocatalysts, a tremendous boost in photodegradation was noted. Additionally, the degradation efficiency of Pt nanoparticles on TiO_2 was tested for comparison. The latter demonstrates poor performance when compared with atomically dispersed Pt atoms; however, all of the Pt-modified samples exhibit a 100% photodegradation efficiency. Due to this robust photodegradation behavior, we compare the overall performance by assessing percent degradation with respect to time (Figure 3b). After 25 min of irradiation, pure TiO_2 degraded 26% of acetaldehyde, which increases to a maximum of 38% in 50 min. When Pt nanoparticles were deposited on TiO_2 (HAADF-STEM: Figure S7), 44 and 83% conversion efficiencies were achieved in 25 and 50 min, respectively. This percent degradation is higher than pure TiO_2; however, it is lower than atomically dispersed Pt-modified TiO_2 samples. The Pt/T 4h sample exhibits 89% of photodegradation efficiency in 25 min, which reaches 96% in 50 min. This photodegradation rate is greater than pure and Pt-modified TiO_2 samples. We additionally evaluate the effect of flow rate on the Pt/T 4h sample (Figure 3c,d). The photodegradation efficiency decreases to 80% with an increasing flow rate, which is associated with a low residence time of the gas molecules on the surface of the photocatalyst. Regardless of this decrease, the photocatalytic activity of Pt/T 4h remains higher than pure TiO_2. The acetaldehyde to CO_2 mineralization test implies that Pt/T 4h is superior to pure TiO_2 (Figure 3e,f). Pure TiO_2 only mineralizes 34% of acetaldehyde, which produces ∼300 ppm of CO_2. Alternatively, Pt/T 4h exhibited a 68.8% mineralization efficiency with around ∼700 ppm of CO_2 released. The cyclic test results reveal that Pt/T 4h is very stable in repeating cycles and show similar behavior without any noticeable change in the photodegradation efficiency (Figure S8). The above results suggest that Pt/T 4h is an excellent photocatalyst exhibiting exceptional activity and stability for the photodegradation of gas-phase acetaldehyde. To understand the role of surface fluorides (F) on the adsorption and photodegradation of pure TiO_2, we first removed the surface F ions by excessive washing. For this purpose, the TiO_2 nanosheets (1 g) were stirred in 0.1 m NaOH solution (100 mL) for 8 h followed by washing with deionized water (3 times). Next, the TiO_2 nanosheets were redispersed in deionized water (100 mL) and 0.1 M HNO_3 was added under stirring for 30 min. Finally, the sample was washed with deionized water three times using centrifugation and dried at 100 °C overnight. The as-processed TiO_2 nanosheets were used to carry out survey XPS (Figure S9), which confirmed the complete removal of the surface F ions. The samples quenched in 0.1 m NaOH without stirring or HNO_3 washing still showed the presence of surface F (Figure S4); thus, we carried out the dynamic adsorption−desorption and photodegradation tests to study the influence of surface F ions. The results are given in Figure S10. It can be seen that there is a slight difference in adsorption and the adsorption curve area of the TiO_2 nanosheets without surface F ions is greater than that of TiO_2 with surface F ions (Figure S10a). Also, the degradation of TiO_2 nanosheets without F ions is a little higher (41%) than that of TiO_2 with surface F ions (38%) (Figure S10b). Although F ions on the surface have been previously accounted for the increasing photocatalytic activity in the open literature, in our study, it did not significantly affect the overall photocatalytic activity.

To study different kinetic parameters, such as the rate constant, water equilibrium constant, and acetaldehyde adsorption constant, we used seven Langmuir−Hinshelwood (L−H) kinetic models for the Pt/T 4h sample. The seven different models are given in Table S2, which are based on different assumptions. The experimental oxidation rate was calculated using the following equation.

$$-r = \frac{F}{V}Xi = \frac{F}{V}\left(\frac{C_{in} - C_{out}}{C_{in}}\right) \quad (1)$$

where r is the reaction rate of acetaldehyde (ppmv min^{-1}), F is the flow rate, V is the volume of the chamber (320 mL), and C_{in} and C_{out} are the inlet and outlet concentrations of acetaldehyde, respectively.

The moisture content in the reaction chamber was determined through a digital hygrometer (10 000 ppmv). The multiple linear regression method was used to fit these models to the experimental data to determine different parameters including the rate constant, k, adsorption equilibrium constant of acetaldehyde, K_A, and adsorption equilibrium constant of water, K_W. The suitability of the

https://doi.org/10.1021/acsanm.1c00208
ACS Appl. Nano Mater. 2021, 4, 3799−3810

models was estimated based on the residual sum of square (RSS) and *R*-squared (R^2) values.

Different parameters determined through these models, are given in Table 1. Model-5 fits well (R^2 = 0.93) with the experimental data from this study. This model assumes that the reaction of VOCs and water occurs on different adsorption sites. The rate of reaction (k) was determined to be 0.1586 ppmv min^{-1}. The adsorption equilibrium constant of acetaldehyde (K_A = 0.7243 $ppmv^{-1}$) is greater than the water equilibrium constant (K_W = 0.000074 $ppmv^{-1}$). It is interesting to note that model-6 does not fit the experimental data, which assumes that the reaction occurs in the gas phase. Thus, it can be concluded that the degradation of acetaldehyde primarily occurred on the catalyst surface. Comparative analysis of these models suggests that the adsorption equilibrium constant of water vapor is smaller than the adsorption equilibrium constant of acetaldehyde. Thus, it can be inferred that acetaldehyde interacted more easily with the surface than water. The competition kinetics suggests that acetaldehyde was adsorbed on most of the active sites on the catalyst's surface. This behavior has been explained in various studies where increasing relative humidity (% RH) results in poor photodegradation performance.[48] Furthermore, low water content has been found to promote the photocatalytic oxidation (PCO) reaction.

The photoinduced holes oxidize the adsorbed water molecules to produce hydroxyl radicals. These •OH radicals act as oxidizing agents in the PCO reaction. However, when the % RH increases to a certain level, the PCO might be affected negatively. This may be due to the competitive adsorption of water and the pollutant gas molecules on the catalyst's surface where some of the water molecules will occupy the active surface sites, e.g., Ti^{4+} in TiO_2.[49] Another possibility is the formation of a film of water molecules on the catalyst's surface, which can impede (reduce) the physical interaction between the VOCs and catalysts.[50] The relative behavior between predicted rates versus experimental rates and the trend of R^2-values for different models are given in Figure 4a,b, respectively. The predicted values are in good agreement with the experimental values for model-5, which strengthens the reliability of the implemented model.

Origin of Improved Photocatalytic Activity. Several tests were carried out to explore the role of Pt on TiO_2 nanosheets. The BET_{SSA} study suggested no significant difference (Table S1 and Figure S11). The BET_{SSA} is recorded as 92.93 to 94.23 $m^2\ g^{-1}$ with a pore diameter of 20.87 to 19.66 nm corresponding to pure TiO_2 and Pt/T 6h samples, respectively. Thus, the surface area is not the fundamental component of high photodegradation performance in this study. The adsorption curves for different samples show no substantial difference in the quantity of gas adsorbed, which is quite predictable based on the BET_{SSA} results (Figure S12a–f). However, the curve area of the Pt-modified samples is slightly higher than that of pure TiO_2. As the interaction between the pollutant gas and the catalyst surface is crucial for the gas–solid reaction, it can be inferred that Pt improved the absorptivity of the acetaldehyde molecules. Also, the Pt/T 6h adsorption area is slightly lower than Pt/T 4h. This might be responsible for the lower degradation of Pt/T 6h contrasted to the Pt/T 4h sample, as well as high wt % of Pt could lead to bigger particles and coverage, although the hole–electron efficiency of Pt/T 6h is higher (photocurrent study; Figure 5e). Thus, 4 h is an optimum deposition time in our work that

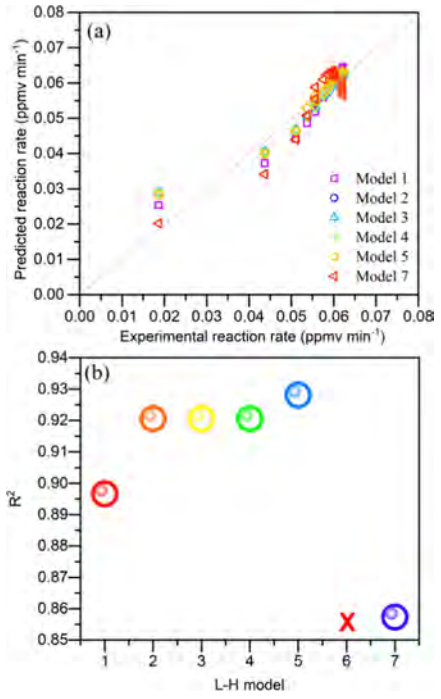

Figure 4. Experimental rate vs predicted rate calculated through Langmuir–Hinshelwood kinetic models (a). Comparative R^2 values that depict the fitting of different Langmuir–Hinshelwood kinetic models to the Pt/T 4h sample (b).

produces overall good photocatalytic performance. The UV–visible results displayed a small shift in the absorption edge toward the higher wavelengths with increasing Pt deposition time (Figure S13a). As an example, the absorption edge of Pt/T 6h shifted more in contrast to pure TiO_2 as well as Pt-modified TiO_2. It could be inferred that Pt decoration on TiO_2 increases the light absorption capability. The band gap values were determined utilizing equation $E = hc/\lambda$ (Table 1), where h (6.626×10^{-34} J s^{-1}) is the Plank constant, c (3.0×10^8 m s^{-1}) is the speed of light, and λ is the cutoff wavelength. The associated UV–visible spectra were used to calculate the absorption edges of different samples. The optical band gap values suggested that the inclusion of Pt on the TiO_2 surface expands the absorption spectrum of TiO_2, and thus, the light-harvesting capability (Table S1). Similar small changes in the absorption edge have been observed previously for similar structures.[40] It has been reported that the interaction of vacancies and Pt atoms might carry out substantial changes in the TiO_2 absorption spectra. For example, Cai et al.[51] studied the effect of Pt doping on the UV–visible spectra of stoichiometric and defective (induced O_v) TiO_2 p25. A significant shift in the visible light absorption was observed for the oxygen vacancy-rich samples. This effect was attributed to the interaction of Pt atoms and oxygen vacancies. In this study, small changes could be associated with the surface modification due to Pt decoration only. The comparative PL spectra of pure and Pt (4h)-modified samples show a broad luminescence spectrum within the range of 350–550 nm (Figure S13b). The broad peak around 400 nm is assigned to the band–band photoluminescence phenomena.[52] The intensity of this peak considerably decreases for Pt/T 4h as opposed to pure TiO_2, suggesting the effective charge separation process under light illumination.[45] Therefore, the optical characterization implies that the light absorption and

https://doi.org/10.1021/acsanm.1c00208
ACS Appl. Nano Mater. 2021, 4, 3799–3810

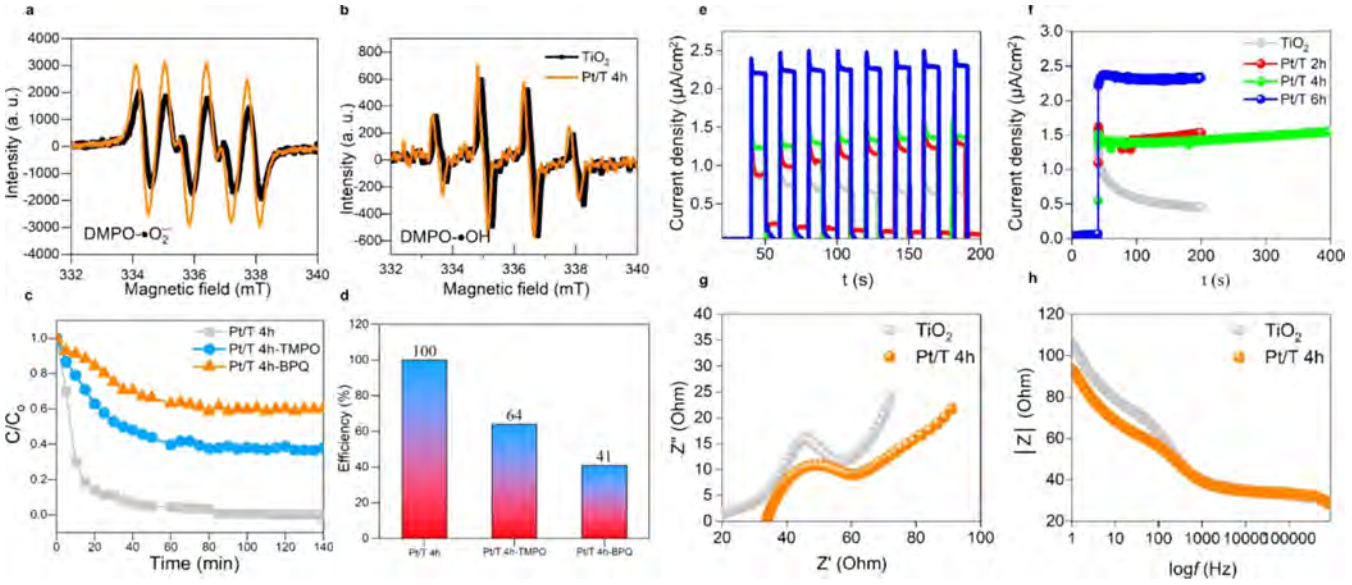

Figure 5. ESR, photocurrent, and electrochemical analysis. ESR spectra of pure TiO_2 and Pt/T 4h nanosheets under UV-light irradiation, DMPO-$^{\bullet}O_2^-$ (a), DMPO-$^{\bullet}OH$ (b), scavenger test (c), photodegradation efficiency in the presence of scavengers (d), current density (μA cm^{-2}) under chopped light (e), current density (μA cm^{-2}) under continuing light illumination (f), Nyquist plots (g), and the Bode plot (h).

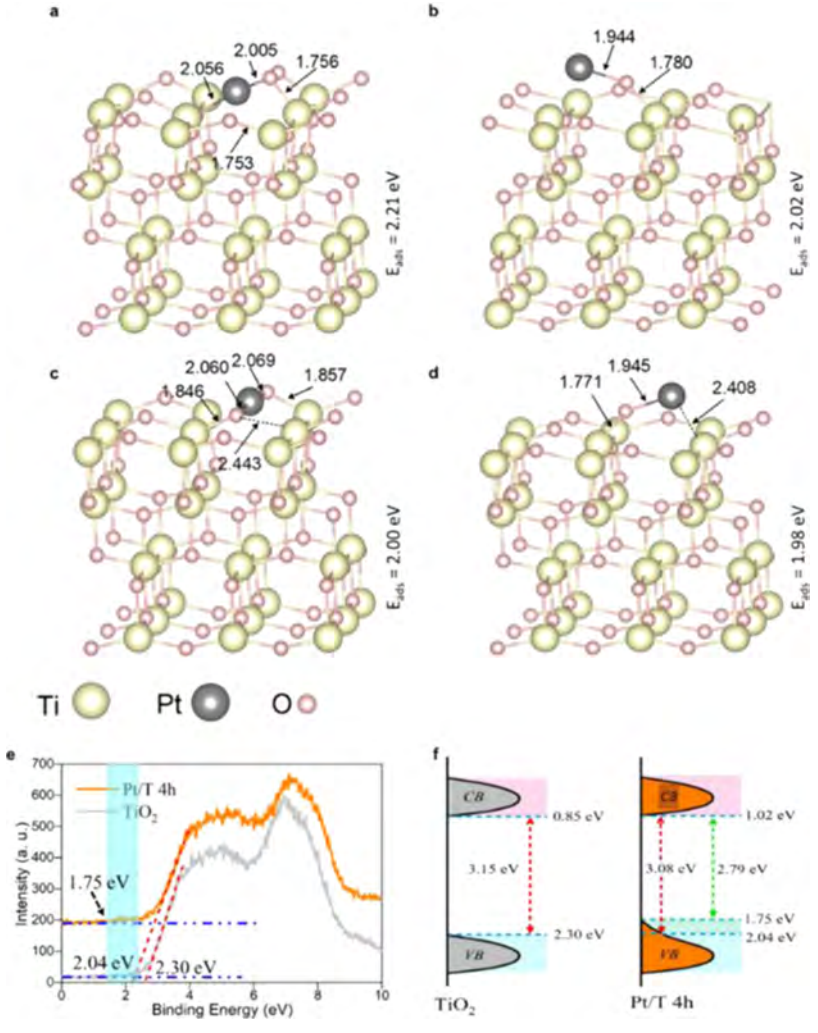

Figure 6. DFT and VB analysis. Adsorption configurations of Pt atoms on the TiO_2(001) surface (a–d), the bond length unit is Å. VB spectra (e) and schematic diagram of DOS of pure TiO_2 and Pt/T 4h samples (f).

https://doi.org/10.1021/acsanm.1c00208
ACS Appl. Nano Mater. 2021, 4, 3799–3810

charge separation potency of TiO_2 is improved by decorating it with Pt. The ESR results reveal that Pt-modified TiO_2 samples exhibit sharp ESR signals, which prove efficient production of $^{\bullet}OH$ and $^{\bullet}O_2^-$ radicals than pure TiO_2 (Figure 5a,b). Thus, it can be inferred that Pt-modified TiO_2 is photocatalytically more active than pure TiO_2 due to the high production of $^{\bullet}OH$ and $^{\bullet}O_2^-$ radicals. The scavenger experiment further determined the role of $^{\bullet}OH$ and $^{\bullet}O_2^-$ radicals (Figure 5c,d). *p*-Benzoquinone (PBQ) and (2,2,6,6-tetramethyl-1-piperidinyloxy (TEMPO) were used to capture the $^{\bullet}O_2^-$ and $^{\bullet}OH$ radicals, respectively. The photodegradation efficiency is observed to decrease (64%) in the presence of TEMPO contrasted to no scavengers (100%). However, when PBQ is used to capture $^{\bullet}O_2^-$ radicals, the photodegradation efficiency (41%) decreases tremendously. These results suggest that both $^{\bullet}OH$ and $^{\bullet}O_2^-$ radicals are crucial for the photodegradation reaction with $^{\bullet}O_2^-$ radicals playing a major role. The transient photocurrent response under chopped conditions further verified the high photodegradation efficiencies of Pt-modified samples (Figure 5e,f). The photocurrent response is greatly improved by increasing the Pt deposition time, for example, the Pt/T 6h sample exhibits a high current density in contrast to pure TiO_2 and other Pt-modified samples. Also, pure TiO_2 exhibits a decreasing photocurrent response with increasing time, while Pt-modified samples exhibit a linear response that is associated with their stability (Figure 5f). The electrochemical impedance and Bode plots further confirm these results (Figure 5g,h).

Detailed periodic DFT calculations were performed to trace the stability and the role of Pt on two distinctive TiO_2 surfaces, which include $TiO_2(101)$ and (001). The configuration in which the Pt atom is attached to the O_{2c} on the $TiO_2(101)$ surface exhibits a high adsorption energy value (Figure S14). The high E_{ads} values (1.55 eV) are calculated for Figure S14d,e modes, where Pt atoms are either attached to two O_{2c} atoms or bonded to O_{2c} and O_{3c}, respectively. These two configurations are the most stable adsorption sites for Pt single atoms on the $TiO_2(101)$ surface. In contrast to the $TiO_2(101)$ surface, the single Pt atoms strongly adsorb on $TiO_2(001)$, which can be attributed to the reactivity of the $TiO_2(001)$ surface that renders it more stable, thus, firmly interacting with the Pt atoms (Figure 6a–d). The E_{ads} values of all configurations are greater than that of $TiO_2(101)$ with E_{ads} = 2.21 eV being the most stable adsorption configuration (Figure 6a). The bond distance between Pt–O_{2c} is 2.005 Å. It has been reported that the stability of Pt atoms on oxide supports depends on the surface atomic arrangement such as under-coordination, surface defects, or existence of active ligands.[53] For example, Kwak et al.[54] studied the anchoring of Pt on γ-Al_2O_3 using an ultrahigh magnetic field, solid-state magic-angle spinning nuclear magnetic resonance spectroscopy, and DFT studies. The results showed that under-coordinated Al^{3+} (pentacoordinate Al^{3+}; Al_{penta}^{3+}) centers on γ-Al_2O_3 {100} facets anchored Pt atoms. The wt % of Pt also affected the morphology of Pt atoms. For example, low Pt content samples exhibited atomically dispersed Pt atoms, while higher coverage resulted in 2D Pt rafts. The DFT results also predict that the affinity of the Pt atoms for different sites on the same surface is quite different. Thus, it is difficult to achieve an entirely uniform morphology of Pt cocatalysts on the TiO_2 surface. However, the synthesis parameters can be optimized to predominantly grow Pt on the TiO_2 surface in a specific morphology.

The calculated band structure and partial density of states (PDOS) of pure and Pt-modified TiO_2 surfaces (101) and (001) are given in Figures S15 and S16, respectively. The calculated band gap value of the pure $TiO_2(101)$ surface is 2.109 eV, which is low in contrast to the experimental value (3.2 eV).[55] However, this is due to the inherent DFT drawback that undermines the electronic band gap.[56] Still, this value is closer to the reported value of the TiO_2 bulk, which confirms the reliability of our surface models.[57] Interestingly, the band gap value of pure $TiO_2(001)$ is much smaller (1.631 eV). This behavior has been observed experimentally, where the optical band gap value of TiO_2 nanoparticles with the dominant (001) surface is lower than that of TiO_2 nanoparticles dominantly grown along the <101> direction.[58] Also, when single Pt atoms are added to the surface, the band gap values are observed to decrease. A significant decrease can be seen in $TiO_2(001)$ (1.147 eV) in comparison to $TiO_2(101)$ (1.279 eV). This shrinkage in the band gap energy will facilitate the light absorption and transfer of electrons between the valence band and the conduction band (CB). The PDOS shows new energy states for the Pt-modified TiO_2 surfaces near the Fermi level (Figure S16c,d). The optical absorption spectra calculated through DFT are presented in Figure S17. With the addition of Pt, the peaks shift to low energy. Additionally, the $TiO_2(001)$ surface shows a peak in the low energy level that is more pronounced with the addition of Pt. Figure 6e,f shows the VB spectra and DOS of pure TiO_2 and Pt/T 4h samples. Pure TiO_2 and Pt/T 4h samples exhibit a VB edge position at 2.30 and 2.04 eV, respectively. Moreover, a band tail is visible in the VB spectrum of the Pt/T 4h sample at around 1.75 eV. Based on the calculated optical band gaps of pure TiO_2 (3.15 eV) and Pt/T 4h (3.05 eV), the corresponding conduction band edge positions are 0.85 and 1.02 eV. The small discrepancy in these values in contrast to previous reports can be attributed to the structural variation of pure TiO_2.[59] These results show that the absorption edge of the Pt/T 4h sample is located at 2.04 eV with an associated band tail of a maximum energy of 1.75 eV. Furthermore, these results suggest that the band gap narrowing occurs in Pt (4h)-modified TiO_2 samples, which are in good agreement with the optical band gap values and periodic DFT results. We further performed ultraviolet photoelectron spectroscopy (UPS) to determine the surface work function of pure TiO_2 nanosheets and the Pt/T 4h sample (Figure 7). The work function of pure TiO_2 is calculated to be 3.9 eV while the work function of Pt/T 4h is determined to be 5.4 eV. It has been reported that a metal–semiconductor junction

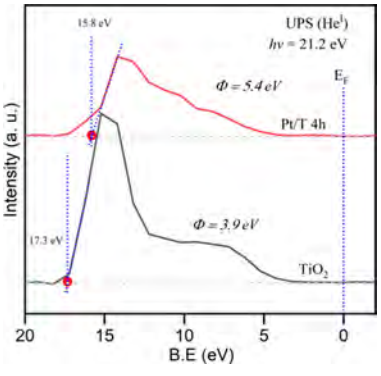

Figure 7. UPS spectra of the valence band of pure TiO_2 nanosheets and Pt/T 4h.

https://doi.org/10.1021/acsanm.1c00208
ACS Appl. Nano Mater. 2021, 4, 3799–3810

could result in the formation of a Schottky junction. In this scenario, the metal catalysts on the oxide surface, e.g., Pt on TiO_2, will work as an electron sink, which will ultimately facilitate the charge separation efficiency due to Schottky barriers.[60] Additionally, the existence of metallic cocatalysts can provide additional active sites on a catalyst surface. Among the various metals, i.e., Au, Cu, Pd, etc., Pt is regarded as the most efficient cocatalyst, which can be attributed to its large work function and lower overpotential toward proton reduction into H_2.[61] The work function of Pt is 5.64 eV vs E_{vacuum} (1.1 eV vs normal hydrogen electrode, NHE), which is positive than the conduction band of TiO_2 (−0.26 eV vs NHE).[62] Thus, it is anticipated that the electrons will transfer from TiO_2 to Pt, which will improve the hole−electron separation process. Additionally, Pt decoration on the surface shifted the VB maximum and CB minimum, which improved light harvesting and charge separation in Pt-modified TiO_2.

CONCLUSIONS

The interaction of metal and oxide supports plays an important role to stabilize and render reactivity to metal cocatalysts. This behavior is more pronounced in atomically dispersed catalysts where the metal−support bonds (metal−metal atomic bonds are weaker than in isolated metals) are relatively stronger. This strong interaction between the metal and oxide support is pivotal in preventing aggregation of the metal atoms. The systematic approach to develop atomically dispersed Pt atoms on TiO_2 nanosheets with the exposed (001) surface has been successfully implemented. Pt-modified TiO_2 nanosheets show a robust and stable photocatalytic activity for the removal of gaseous acetaldehyde. Also, atomically dispersed Pt atoms exhibited higher photocatalytic activity than Pt nanoparticles. The experimental results and periodic DFT calculations reveal that the Pt atoms are more stable on the TiO_2(001) surface than the (101) surface. Pt exhibits a poor interaction with TiO_2(101) and likely results in aggregation and formation of Pt clusters. The aggregation of Pt atoms into clusters and nanoparticles occurs due to the insufficient anchoring effect of the support to Pt atoms. Two fundamental properties are improved, i.e., charge separation efficiency and light-harvesting capability, which are responsible for the enhanced photocatalytic performance. Also, the adsorption capability was observed to improve for the Pt-modified samples when compared to pure TiO_2. Our results suggest that decorating TiO_2 nanoparticles with atomically dispersed Pt will lead to an efficient and stable photocatalyst that can be used for the removal of indoor air pollutants. This study explores in detail the role of Pt on TiO_2 nanosheets and its potency for the photocatalytic degradation of low content gas-phase acetaldehyde, which may be extended to different kinds of VOCs in the future.

ASSOCIATED CONTENT

Supporting Information

The Supporting Information is available free of charge at https://pubs.acs.org/doi/10.1021/acsanm.1c00208.

Crystal parameters, BET_{SSA} analysis, and optical bandgap of pure and Pt modified TiO_2 (Table S1); Langmuir-Hinshelwood kinetic models based on different assumptions (Table S2); percentage of exposed (001) surface, average length (a) and thickness (b) calculated for the pure TiO_2 nanosheets (Figure S1); size distribution of Pt (4 h) on TiO_2 nanosheets (Figure S2); HAADF-STEM image of TiO_2 nanosheets without surface F ions (Figure S3); survey XPS spectra of pure and Pt (4h) modified TiO_2 nanosheets (Figure S4); electron paramagnetic spectrum (EPR) of pure and Pt decorated TiO_2 (Figure S5); schematic view of the dynamic adsorption-desorption and photocatalytic test systems (Figure S6); HAADF-STEM image of Pt nanoparticles on TiO_2 nanosheets (Figure S7); cyclic stability test of the Pt/T 4h sample under repetitive cycles (Figure S8); survey XPS spectrum of pure TiO_2 nanosheets after stirring in 0.1 M NaOH (8 h) and HNO3 treatment for 30 minutes (Figure S9); adsorption and degradation curve (Figure S10); nitrogen adsorption−desorption isotherm (a) and pore diameter (b) of pure and Pt modified TiO_2 nanosheets (Figure S11); adsorption efficiency and corresponding area calculated for the pure and Pt modified TiO_2 nanosheets (Figure S12); optical characterization (Figure S13); Adsorption configurations of Pt single atom on TiO_2(101) surface (Figure S14); band structure of pure and Pt single atom decorated TiO_2 surfaces (Figure S15); PDOS of pure and Pt single atom decorated TiO_2 surfaces (Figure S16); absorption spectra as a function of photon energy for the pure and Pt modified TiO_2(101) and (001) surfaces (Figure S17) (PDF)

AUTHOR INFORMATION

Corresponding Authors

Asad Mahmood − *Shanghai Institute of Ceramics, Chinese Academy of Sciences, Shanghai 200050, China;* orcid.org/0000-0002-5866-0680; Phone: +86-15618737781; Email: amkhan036@yahoo.com

Jing Sun − *Shanghai Institute of Ceramics, Chinese Academy of Sciences, Shanghai 200050, China;* orcid.org/0000-0003-1101-1584; Phone: +86-(0)21-5241 2717; Email: jingsun@mail.sic.ac.cn

Authors

Xiao Wang − *Shanghai Institute of Ceramics, Chinese Academy of Sciences, Shanghai 200050, China;* orcid.org/0000-0001-9786-8153

Xiaofeng Xie − *Shanghai Institute of Ceramics, Chinese Academy of Sciences, Shanghai 200050, China;* orcid.org/0000-0003-1789-1084

Complete contact information is available at: https://pubs.acs.org/10.1021/acsanm.1c00208

Author Contributions

A.M. designed the experiments. A.M., X.W., and X.X. performed all of the experiments and analyzed the data with contributions from J.S. A.M. performed the synthesis, photocatalytic tests, phase and microstructure analysis, and DFT calculations. X.W. performed XPS and ESR analysis. X.X. and J.S. contributed to photocatalytic tests and HAADF-STEM analysis. All authors contributed to the interpretation of the results and writing of the manuscript.

Notes

The authors declare no competing financial interest.

https://doi.org/10.1021/acsanm.1c00208
ACS Appl. Nano Mater. 2021, 4, 3799−3810

■ ACKNOWLEDGMENTS

This work was financially supported by the National Key Research and Development Program of China (2016YFA0203000), Shanghai Commission of Science and Technology Program (19DZ1202600 and 20DZ1204100), the National Natural Science Foundation of China (Grant No. 41907303), and the Innovation Fund of SICCAS (No. Y91ZC5150G).

■ REFERENCES

(1) Agency, E. E. *Air Quality in Europe—2019 Report*; 2019; pp 1–104.
(2) Héquet, V.; Raillard, C.; Debono, O.; Thévenet, F.; Locoge, N.; Le Coq, L. Photocatalytic Oxidation of VOCs at ppb Level Using a Closed-Loop Reactor: The Mixture Effect. *Appl Catal., B* **2018**, *226*, 473–486.
(3) Suárez, S.; Jansson, I.; Ohtani, B.; Sánchez, B. From Titania Nanoparticles to Decahedral Anatase Particles: Photocatalytic Activity of TiO_2/Zeolite Hybrids for VOCs Oxidation. *Catal. Today* **2019**, *326*, 2–7.
(4) Mustafa, M. F.; Fu, X.; Liu, Y.; Abbas, Y.; Wang, H.; Lu, W. Volatile Organic Compounds (VOCs) Removal in Non-Thermal Plasma Double Dielectric Barrier Discharge Reactor. *J. Hazard. Mater.* **2018**, *347*, 317–324.
(5) Xiang, W.; Zhang, X.; Chen, K.; Fang, J.; He, F.; Hu, X.; Tsang, D. C. W.; Ok, Y. S.; Gao, B. Enhanced Adsorption Performance and Governing Mechanisms of Ball-Milled Biochar for the Removal of Volatile Organic Compounds (VOCs). *Chem. Eng. J.* **2020**, *385*, No. 123842.
(6) Mahmood, A.; Wang, X.; Shi, G.; Wang, Z.; Xie, X.; Sun, J. Revealing Adsorption and the Photodegradation Mechanism of Gas Phase *o*-Xylene on Carbon Quantum Dots Modified TiO_2 Nanoparticles. *J. Hazard. Mater.* **2019**, *386*, No. 121962.
(7) Zhang, Y.; Tang, Z.-R.; Fu, X.; Xu, Y.-J. TiO_2-Graphene Nanocomposites for Gas-Phase Photocatalytic Degradation of Volatile Aromatic Pollutant: Is TiO_2-Graphene Truly Different From Other TiO_2-Carbon Composite Materials? *ACS Nano* **2010**, *4*, 7303–7314.
(8) Zeng, M.; Li, Y.; Mao, M.; Bai, J.; Ren, L.; Zhao, X. Synergetic Effect Between Photocatalysis on TiO_2 And Thermocatalysis on CeO_2 For Gas-Phase Oxidation of Benzene on TiO_2/CeO_2 Nanocomposites. *ACS Catal.* **2015**, *5*, 3278–3286.
(9) Wang, C.; Xi, J. Y.; Hu, H. Y.; Yao, Y. Advantages of Combined UV Photodegradation and Biofiltration Processes to Treat Gaseous Chlorobenzene. *J. Hazard. Mater.* **2009**, *171*, 1120–5.
(10) Zeng, Q.; Wang, X.; Xie, X.; Mahmood, A.; Lu, G.; Wang, Y.; Sun, J. Band Bending of TiO_2 induced by *o*-Xylene And Acetaldehyde Adsorption and Its Effect on the Generation of Active radicals. *J. Colloid Interface Sci.* **2020**, *572*, 374–383.
(11) Wang, W.; Yu, J.; Xiang, Q.; Cheng, B. Enhanced Photocatalytic Activity of Hierarchical Macro/Mesoporous TiO_2–Graphene Composites for Photodegradation of Acetone in Air. *Appl. Catal., B* **2012**, *119-120*, 109–116.
(12) Wang, J.; Xu, X.; Cao, F.; Wang, Y.; Li, S.; Qin, G. In Situ Fabrication of α-Fe_2O_3/$CaFe_2O_4$ p-n Heterojunction With Enhanced VOCs Photodegradation Activity. *Adv. Powder Technol.* **2019**, *30*, 590–595.
(13) Chen, X.; Yu, C.; Zhu, R.; Li, N.; Chen, J.; Lin, Q.; Xu, S.; Chen, X.; Wang, H. Photocatalytic Performance and Mechanism of Z-Scheme $CuBi_2O_4$/Ag_3PO_4 in the Degradation of Diclofenac Sodium Under Visible Light Irradiation: Effects of pH, H_2O_2, and S_2O_8(2). *Sci. Total Environ.* **2020**, *711*, No. 134643.
(14) Meng, Y.; Dai, T.; Zhou, X.; Pan, G.; Xia, S. Photodegradation of Volatile Organic Compounds Catalyzed by MCr-LDHs and Hybrid MO@MCr-LDHs (M = Co, Ni, Cu, Zn): The Comparison of Activity, Kinetics and Photocatalytic Mechanism. *Catal. Sci. Technol.* **2020**, *10*, 424–439.
(15) Pradhan, A. C.; Uyar, T. Electrospun Fe_2O_3 Entrenched SiO_2 Supported N and S Dual Incorporated TiO_2 Nanofibers Derived from Mixed Polymeric Template/Surfactant: Enriched Mesoporosity within Nanofibers, Effective Charge Separation, and Visible Light Photocatalysis Activity. *Ind. Eng. Chem. Res.* **2019**, *58*, 12535–12550.
(16) Huang, Y.; Liang, Y.; Rao, Y.; Zhu, D.; Cao, J. J.; Shen, Z.; Ho, W.; Lee, S. C. Environment-Friendly Carbon Quantum Dots/$ZnFe_2O_4$ Photocatalysts: Characterization, Biocompatibility, and Mechanisms for NO Removal. *Environ. Sci. Technol.* **2017**, *51*, 2924–2933.
(17) Zhang, Z.; Zhu, Y.; Asakura, H.; Zhang, B.; Zhang, J.; Zhou, M.; Han, Y.; Tanaka, T.; Wang, A.; Zhang, T.; Yan, N. Thermally Stable Single Atom Pt/m-Al_2O_3 for Selective Hydrogenation and CO Oxidation. *Nat. Commun.* **2017**, *8*, No. 16100.
(18) Sanzone, G.; Zimbone, M.; Cacciato, G.; Ruffino, F.; Carles, R.; Privitera, V.; Grimaldi, M. G. Ag/TiO_2 Nanocomposite for Visible Light-Driven Photocatalysis. *Superlattices Microstruct.* **2018**, *123*, 394–402.
(19) Li, X.; Bi, W.; Zhang, L.; Tao, S.; Chu, W.; Zhang, Q.; Luo, Y.; Wu, C.; Xie, Y. Single-Atom Pt as Co-catalyst for Enhanced Photocatalytic H_2 Evolution. *Adv. Mater.* **2016**, *28*, 2427–31.
(20) Stucchi, M.; Bianchi, C. L.; Argirusis, C.; Pifferi, V.; Neppolian, B.; Cerrato, G.; Boffito, D. C. Ultrasound Assisted Synthesis of Ag-Decorated TiO_2 Active in Visible Light. *Ultrason. Sonochem* **2018**, *40*, 282–288.
(21) Stucchi, M.; Cerrato, G.; Bianchi, C. L. Ultrasound to Improve Both Synthesis and Pollutants Degradation Based on Metal Nanoparticles Supported on TiO_2. *Ultrason. Sonochem.* **2019**, *51*, 462–468.
(22) Macino, M.; Barnes, A. J.; Althahban, S. M.; Qu, R.; Gibson, E. K.; Morgan, D. J.; Freakley, S. J.; Dimitratos, N.; Kiely, C. J.; Gao, X.; Beale, A. M.; Bethell, D.; He, Q.; Sankar, M.; Hutchings, G. J. Tuning of Catalytic Sites in Pt/TiO_2 Catalysts for the Chemoselective Hydrogenation of 3-Nitrostyrene. *Nat. Catal.* **2019**, *2*, 873–881.
(23) Huang, H.; Leung, D. Y. C.; Ye, D. Effect of Reduction Treatment on Structural Properties of TiO_2 Supported Pt Nanoparticles and their Catalytic Activity for Formaldehyde Oxidation. *J. Mater. Chem.* **2011**, *21*, 9647–9652.
(24) Kim, M.-S.; Kim, J. S.; Kim, B.-W. Removal of Gaseous Toluene by Using TiO_2 Film Doped of Ru-dye/Pt in a Pilot Scale Photoreactor. *Korean J. Chem. Eng.* **2012**, *29*, 549–554.
(25) Pan, J.; Liu, G.; Lu, G. Q.; Cheng, H. M. On the True Photoreactivity Order of {001}, {010}, and {101} Facets of Anatase TiO_2 crystals. *Angew. Chem., Int. Ed.* **2011**, *50*, 2133–2137.
(26) Peng, C.; Yang, X.; Li, Y.; Yu, H.; Wang, H.; Peng, F. Hybrids of Two-Dimensional Ti_3C_2 and TiO_2 Exposing {001} Facets Toward Enhanced Photocatalytic Activity. *ACS Appl. Mater. Interface.* **2016**, *8*, 6051–60.
(27) Yu, J.; Low, J.; Xiao, W.; Zhou, P.; Jaroniec, M. Enhanced Photocatalytic CO_2-Reduction Activity of Anatase TiO_2 by Coexposed {001} and {101} Facets. *J. Am. Chem. Soc.* **2014**, *136*, 8839–42.
(28) Stefanov, B. I.; Topalian, Z.; Granqvist, C. G.; Österlund, L. Acetaldehyde Adsorption and Condensation on Anatase TiO_2: Influence of Acetaldehyde Dimerization. *J. Mol. Catal. A: Chem.* **2014**, *381*, 77–88.
(29) EPA. *Office of Air Quality Planning and Standards (QAQPS)*; Research Triangle Park: NC, USA, 2002.
(30) Kresse, G.; Hafner, J. Ab Initiomolecular Dynamics for Liquid Metals. *Phys. Rev. B* **1993**, *47*, 558–561.
(31) Kresse, G.; Furthmuller, J. Efficiency of Ab-Initio Total Energy Calculations for Metals and Semiconductors Using a Plane-Wave Basis Set. *Comput. Mater. Sci.* **1996**, *6*, 15–50.
(32) Kresse, G.; Furthmuller, J. Efficient Iterative Schemes for Ab Initio Total-Energy Calculations Using a Plane-Wave Basis Set. *Phys. Rev. B* **1996**, *54*, No. 11169.
(33) Perdew, J. P.; Burke, K.; Ernzerhof, M. Generalized Gradient Approximation Made Simple. *Phys. Rev. Lett.* **1996**, *77*, 3865–3868.

https://doi.org/10.1021/acsanm.1c00208
ACS Appl. Nano Mater. 2021, 4, 3799–3810

(34) Grimme, S. Semiempirical GGA-Type Density Functional Constructed with a Long-Range Dispersion Correction. *J. Comput. Chem.* **2006**, *27*, 1787−1799.
(35) Shi, G.; Mahmood, A.; Lu, G.; Wang, X.; Tong, S.; Ge, M.; Xie, X.; Sun, J. Adsorption and Photodegradation of Acetaldehyde and Ethylene on TiO_2(001) Surface: Experimental and First Principle Studies. *Catal. Lett.* **2019**, *149*, 2728−2738.
(36) Scarisoreanu, M.; Ilie, A. G.; Goncearenco, E.; Banici, A. M.; Morjan, I. P.; Dutu, E.; Tanasa, E.; Fort, I.; Stan, M.; Mihailescu, C. N.; Fleaca, C. Ag, Au and Pt decorated TiO_2 Biocompatible Nanospheres for UV & Vis Photocatalytic Water Treatment. *Appl. Surf. Sci.* **2020**, *509*, No. 145217.
(37) Li, C.; Koenigsmann, C.; Ding, W.; Rudshteyn, B.; Yang, K. R.; Regan, K. P.; Konezny, S. J.; Batista, V. S.; Brudvig, G. W.; Schmuttenmaer, C. A.; Kim, J. H. Facet-Dependent Photoelectrochemical Performance of TiO_2 Nanostructures: An Experimental and Computational Study. *J. Am. Chem. Soc.* **2015**, *137*, 1520−1529.
(38) Kwak, J. H.; Hu, J.; Mei, D.; Yi, C.-W.; Kim, D. H.; Peden, C. H. F.; Allard, L. F.; Szanyi, J. Coordinatively Unsaturated Al^{3+} Centers as Binding Sites for Active Catalyst Phases of Platinum on Gamma-Al_2O_3. *Science* **2009**, *325*, 1670−1673.
(39) Bharti, B.; Kumar, S.; Lee, H. N.; Kumar, R. Formation of Oxygen Vacancies and Ti(3+) State in TiO_2 Thin Film and Enhanced Optical Properties by Air Plasma Treatment. *Sci. Rep.* **2016**, *6*, No. 32355.
(40) Wei, T.; Zhu, Y.; Wu, Y.; An, X.; Liu, L. M. Effect of Single-Atom Cocatalysts on the Activity of Faceted TiO_2 Photocatalysts. *Langmuir* **2019**, *35*, 391−397.
(41) Wan, J.; Chen, W.; Jia, C.; Zheng, L.; Dong, J.; Zheng, X.; Wang, Y.; Yan, W.; Chen, C.; Peng, Q.; Wang, D.; Li, Y. Defect Effects on TiO_2 Nanosheets: Stabilizing Single Atomic Site Au and Promoting Catalytic Properties. *Adv. Mater.* **2018**, *30*, No. 1705369.
(42) Rutar, M.; Rozman, N.; Pregelj, M.; Bittencourt, C.; Cerc Korosec, R.; Sever Skapin, A.; Mrzel, A.; Skapin, S. D.; Umek, P. Transformation of Hydrogen Titanate Nanoribbons to TiO_2 Nanoribbons and the Influence of the Transformation Strategies on the Photocatalytic Performance. *Beilstein J. Nanotechnol.* **2015**, *6*, 831−844.
(43) Zhang, X.; Wang, L.; Chen, S.; Huang, Y.; Song, Z.; Yu, M. Facile Synthesis and Enhanced Visible-Light Photocatalytic Activity of Ti^{3+}-doped TiO_2 Sheets with Tunable Phase Composition. *Front. Chem. Sci. Eng.* **2015**, *9*, 349−358.
(44) Li, G.; Dimitrijevic, N. M.; Chen, L.; Nichols, J. M.; Rajh, T.; Gray, K. A. The Important Role of Tetrahedral Ti^{4+} Sites in the Phase Transformation and Photocatalytic Activity of TiO_2 Nanocomposites. *J. Am. Chem. Soc.* **2008**, *130*, 5402−5403.
(45) Lin, W.; Xie, X.; Wang, X.; Wang, Y.; Segets, D.; Sun, J. Efficient Adsorption and Sustainable Degradation of Gaseous Acetaldehyde and *o*-Xylene Using rGO-TiO_2 Photocatalyst. *Chem. Eng. J.* **2018**, *349*, 708−718.
(46) Shi, Y.; Chen, J.; Mao, Z.; Fahlman, B. D.; Wang, D. Construction of Z-Scheme Heterostructure with Enhanced Photocatalytic H_2 Evolution for g-C_3N_4 Nanosheets via Loading Porous Silicon. *J. Catal.* **2017**, *356*, 22−31.
(47) Wang, F.; Wu, Y.; Wang, Y.; Li, J.; Jin, X.; Zhang, Q.; Li, R.; Yan, S.; Liu, H.; Feng, Y.; Liu, G.; Lv, W. Construction of Novel Z-scheme Nitrogen-Doped Carbon Dots/{0 0 1} TiO_2 Nanosheet Photocatalysts for Broad-Spectrum-Driven Diclofenac Degradation: Mechanism Insight, Products and Effects of Natural Water Matrices. *Chem. Eng. J.* **2019**, *356*, 857−868.
(48) Mamaghani, A. H.; Haghighat, F.; Lee, C.-S. Gas Phase Adsorption of Volatile Organic Compounds onto Titanium Dioxide Photocatalysts. *Chem. Eng. J.* **2018**, *337*, 60−73.
(49) Quici, N.; Vera, M. L.; Choi, H.; Puma, G. L.; Dionysiou, D. D.; Litter, M. I.; Destaillats, H. Effect of Key Parameters on the Photocatalytic Oxidation of Toluene at Low Concentrations in Air Under 254+185nm UV irradiation. *Appl. Catal., B* **2010**, *95*, 312−319.
(50) Mamaghani, A. H.; Haghighat, F.; Lee, C.-S. Photocatalytic Degradation of VOCs on Various Commercial Titanium Dioxides: Impact of Operating Parameters on Removal Efficiency and By-Products Generation. *Build. Environ.* **2018**, *138*, 275−282.
(51) Cai, S.; Wang, L.; Heng, S.; Li, H.; Bai, Y.; Dang, D.; Wang, Q.; Zhang, P.; He, C. Interaction of Single-Atom Platinum−Oxygen Vacancy Defects for the Boosted Photosplitting Water H_2 Evolution and CO_2 Photoreduction: Experimental and Theoretical Study. *J. Phys. Chem. C* **2020**, *124*, 24566−24579.
(52) Mahmood, A.; Shi, G.; Xie, X.; Sun, J. Assessing the Adsorption and Photocatalytic Activity of TiO_2 Nanoparticles for the Gas Phase Acetaldehyde: A Computational and Experimental Study. *J. Alloys Compd.* **2020**, *819*, No. 153055.
(53) Thang, H. V.; Pacchioni, G.; DeRita, L.; Christopher, P. Nature of Stable Single Atom Pt Catalysts Dispersed on Anatase TiO_2. *J. Catal.* **2018**, *367*, 104−114.
(54) Kwak, J. H.; Hu, J.; Mei, D.; Yi, C.-W.; Kim, D. H.; Peden, C. H. F.; Allard, L. F.; Szanyi, J. Coordinatively Unsaturated Al^{3+} Centers as Binding Sites for Active Catalyst Phases of Platinum on γ-Al_2O_3. *Science* **2009**, *325*, 1640−1673.
(55) Zeng, Q.; Xie, X.; Wang, X.; Wang, Y.; Lu, G.; Pui, D. Y. H.; Sun, J. Enhanced Photocatalytic Performance of Ag@TiO_2 for the Gaseous Acetaldehyde Photodegradation Under Fluorescent Lamp. *Chem. Eng. J.* **2018**, *341*, 83−92.
(56) Wang, Y.; Zhang, R.; Li, J.; Li, L.; Lin, S. First-Principles Study on Transition Metal-Doped Anatase TiO_2. *Nanoscale Res. Lett.* **2014**, *9*, No. 46.
(57) Samat, M. H.; Ali, A. M. M.; Taib, M. F. M.; Hassan, O. H.; Yahya, M. Z. A. Structural and Electronic Properties of TiO_2 Polymorphs with Effective on-site Coulomb Repulsion Term: DFT +U Approaches. *Mater. Today: Proc.* **2019**, *17*, 472−483.
(58) Chen, M.; Ma, J.; Zhang, B.; Wang, F.; Li, Y.; Zhang, C.; He, H. Facet-Dependent Performance of Anatase TiO_2 for Photocatalytic Oxidation of Gaseous Ammonia. *Appl. Catal., B* **2018**, *223*, 209−215.
(59) Matsuda, A.; Sreekantan, S.; Krengvirat, W. Well-Aligned TiO_2 Nanotube Arrays for Energy-Related Applications Under Solar Irradiation. *J. Asian Ceram. Soc.* **2018**, *1*, 203−219.
(60) Meng, A.; Zhang, L.; Cheng, B.; Yu, J. Dual Cocatalysts in TiO_2 Photocatalysis. *Adv. Mater.* **2019**, *31*, No. e1807660.
(61) Wang, F.; Jiang, Y.; Lawes, D. J.; Ball, G. E.; Zhou, C.; Liu, Z.; Amal, R. Analysis of the Promoted Activity and Molecular Mechanism of Hydrogen Production over Fine Au−Pt Alloyed TiO_2 Photocatalysts. *ACS Catal.* **2015**, *5*, 3924−3931.
(62) Meng, A.; Zhang, J.; Xu, D.; Cheng, B.; Yu, J. Enhanced photocatalytic H_2-Production Activity of Anatase TiO_2 Nanosheet by Selectively Depositing Dual-Cocatalysts on {101} and {001} Facets. *Appl. Catal., B* **2016**, *198*, 286−294.

https://doi.org/10.1021/acsanm.1c00208
ACS Appl. Nano Mater. 2021, 4, 3799−3810